ROYAL SOCIETY
OF CHEMISTRY

PAPER

Check for updates

Adsorption, activation, and conversion of carbon dioxide on small copper–tin nanoclusters†

Akshayini Muthuperiyanayagam,[a] Azeem Ghulam Nabi,[abc] Qi Zhao, [ID] [a]
Aman-ur-Rehman[bde] and Devis Di Tommaso [ID] *[a]

Carbon dioxide (CO_2) conversion to value-added chemicals is an attractive solution to reduce globally accelerating CO_2 emissions. Among the non-precious and abundant metals tested so far, copper (Cu) is one of the best electrocatalysts to convert CO_2 into more than thirty different hydrocarbons and alcohols. However, the selectivity for desired products is often too low. We present a computational investigation of the effects of nanostructuring, doping, and support on the activity and selectivity of Cu–Sn catalysts. Density functional theory calculations were conducted to explore the possibility of using small Cu–Sn clusters, $Cu_{4-n}Sn_n$ (n = 0–4), isolated or supported on graphene and γ-Al_2O_3, to activate CO_2 and convert it to carbon monoxide (CO) and formic acid (HCOOH). First, a detailed analysis of the structure, stability, and electronic properties of $Cu_{4-n}Sn_n$ clusters and their ability to absorb and activate CO_2 was considered. Then, the kinetics of the gas phase CO_2 direct dissociation on $Cu_{4-n}Sn_n$ to generate CO was determined. Finally, the mechanism of electrocatalytic CO_2 reduction to CO and HCOOH on $Cu_{4-n}Sn_n$, $Cu_{4-n}Sn_n$/graphene and $Cu_{4-n}Sn_n$/γ-Al_2O_3 was computed. The selectivity towards the competitive electrochemical hydrogen evolution reaction on these catalysts was also considered. The Cu_2Sn_2 cluster suppresses the hydrogen evolution reaction and is highly selective towards CO, if unsupported, or HCOOH if supported on graphene. This study demonstrates that the Cu_2Sn_2 cluster is a potential candidate for the electrocatalytic conversion of the CO_2 molecule. Moreover, it identifies insightful structure–property relationships in Cu-based nanocatalysts, highlighting the influence of composition and catalyst support on CO_2 activation.

[a] *Department of Chemistry, School of Physical and Chemical Sciences,*
Queen Mary University of London, Mile End Road, London, E1 4NS, UK.
E-mail: d.ditommaso@qmul.ac.uk

[b] *Department of Physics and Applied Mathematics, Pakistan Institute of Engineering*
& Applied Sciences, P.O. Nilore, Islamabad, 45650, Pakistan

[c] *Department of Physics, University of Gujrat, Jalalpur Jattan Road, Gujrat, Pakistan*

[d] *Department of Nuclear Engineering, Pakistan Institute of Engineering & Applied*
Sciences, Nilore, Islamabad 45650, Pakistan

[e] *Center for Mathematical Sciences, Pakistan Institute of Engineering & Applied*
Sciences, Nilore, Islamabad 45650, Pakistan

† Electronic supplementary information (ESI) available: (i) Energies, zero-point energies, and entropies of $H_2(g)$, $CO_2(g)$, and $CO(g)$. (ii) Configurations of the initial state, transition state, and final state involved in CO_2 direct dissociation to CO ($CO_2^* \rightarrow CO^* + O^*$) over Cu_4, Cu_3Sn, Cu_2Sn_2, and $CuSn_3$. (iii) Configurations of the intermediates OCHO*, COOH*, and *CO involved in the CO_2 reduction reactions over Cu_4, Cu_3Sn, Cu_2Sn_2, and $CuSn_3$. (iv) CO_2 adsorption, activation and reduction reaction on the isomers of Cu_3Sn. See DOI: https://doi.org/10.1039/d3cp00477e

1. Introduction

The increasing carbon dioxide (CO_2) level in the environment is the main contributor to global warming.[1] The global temperature has increased by 1 °C compared to the pre-industrial era and will increase by a further 1.5 °C within the next two decades.[2] One of the solutions is CO_2 utilization, that is, the conversion of captured CO_2 to value-added materials and chemicals.[3] CO_2 conversion is a flourishing area of research as it could use CO_2 as a virtually illimited source of carbon feedstock material. One of the most promising approaches is the electrochemical CO_2 reduction (eCO_2R) to other C_1 products such as formic acid (HCOOH) and carbon monoxide (CO), and C_{2+} substances such as ethylene, ethanol, and others.[2,3] The main challenge in eCO_2R research lies in the activation of CO_2 minimizing competitive pathways such as the hydrogen evolution reaction (HER, $H^+ + e^- \rightarrow 1/2H_2$). Thus, catalysts are indispensable for accelerating the eCO_2R process to recycle CO_2 to value-added chemicals with high faradaic efficiency (FE).

Copper (Cu) is the only metal surface that reduces CO_2 to more than thirty different hydrocarbons and oxygenates.[4] For this reason, Cu is considered the best candidate for eCO_2R but lacks the required selectivity. For example, the FE achieved for ethylene, the simplest of the C_2 products, is no more than 40% at 200 mA cm^{-2},[5] still too low for practical application.[6] However, the synthesis of small nanoclusters, Cu_n (n = 3, 4, 8, 20),

This journal is © the Owner Societies 2023

Phys. Chem. Chem. Phys., 2023, **25**, 13429–13441 | **13429**

supported on alumina (Al_2O_3) exhibited high turnover for the CO_2 conversion to methanol.[7,8] Larger Cu nanoclusters (1.24 nm) also showed a high FE of 93.5% at −0.50 V (RHE) for CO_2 reduction to CO.[9] A complementary approach to nanostructuring is the incorporation of a second metal[10] to alter the electronic structure (ligand and strain effects)[11] of the host material and the atomic arrangement (geometric ensemble effects) of the active sites. Metal doping can result in the introduction of new actives sites in the bimetallic catalyst that are not present in its mono-metallic counterparts. Experimental results also showed that the activity and selectivity of eCO_2R to HCOOH and CO can be enhanced by incorporating metals such as gold (Au), indium (In), palladium (Pd), cobalt (Co), tungsten (W), and tin (Sn).[12] Au, In and Pd are expensive and/or scarce, whereas Co and W are toxic. Earth-abundant and non-toxic metals such as Sn would be the preferred option for a long-term Cu-based sustainable catalyst solution to eCO_2R. The use of Sn is also attractive because of its high selectivity toward C_1 products.[13] Cu–Sn catalysts suppress the HER by weakening the binding strength of H and show selectivity for formate ($HCOO^-$) or CO depending on the Cu/Sn ratio.[14] In this regard, a techno-economic evaluation of low-temperature CO_2 electrolysis showed that achieving high yields of C_1 products such as HCOOH and CO is competitive to conventional processes compared to achieving C_2 products, whose production has substantially higher costs.[15] Consequently, significant progress in the electrochemical CO_2 reduction to C_1 products could be achieved using Cu-based alloy clusters doped with earth-abundant metals such as Sn.

The use of small four-atom Cu clusters, Cu_4, as catalysts for the conversion of CO_2, to not only methanol but also other several chemicals, has been reported in several experimental and theoretical studies.[7,8,16–18] Previous computational work focused on tetrahedral non-supported bimetallic Cu–Pt,[19] Cu–Pd and Cu–Ni,[20] and Cu–Zr.[21] But there is still a lack of understanding regarding the effect of the inclusion of Sn atoms in small copper clusters. Moreover, in the realistic electrocatalytic reaction, a cluster is supported by oxides and other substrates. Lee et al. studied CO_2 conversion on Fe–Cu–K catalysts supported on various oxides, such as Al_2O_3, SiO_2, and TiO_2, and found that alumina enhances CO_2 chemisorption and, therefore, its activation.[9] Another study found stable Cu nanoclusters (n = 3, 4, 8, 20 and so forth) synthesized on alumina (Al_2O_3) to be active towards CO_2 conversion to methanol.[7] Similarly, Cu_4 deposited on Al_2O_3 exhibited a high turnover for catalytic CO_2 hydrogenation.[8] A density functional theory (DFT) study of CO_2 adsorption on Cu–Co clusters supported on partially hydroxylated Al_2O_3 showed that CO_2 interacts not only with the catalysts but also with the support via hydrogen bond with the hydroxyl group or direct bonding of the O atoms of the alumina surface.[22] This process stabilizes and activates the adsorbed CO_2 species (elongated C–O bonds and reduced O–C–O angle). Apart from metal oxides, graphene, a 2D material, has been used to disperse Cu clusters for the eCO_2R to C_1 products.[23] Anchoring Cu atoms over defective diamond graphene showed high catalytic activity for the

selective conversion of acetylene to ethylene.[24] Nitrogen-doped (ND) graphene-supported gold clusters catalyse the CO_2 electroreduction to CO.[25] Experimental work showed the efficient formation of two-carbon (C_2) products on small Cu clusters embedded in mesoporous carbon spheres,[26] metal-organic frameworks or Cu-coordinated polymers.[27,28] Li et al. studied the catalytic activity of small copper clusters anchored over defective nanodiamond graphene for CO_2 reduction and found Cu_3/ND@graphene and Cu_4/ND@graphene to convert CO_2 to C_1 compounds.[29]

On this basis, we present a systematic computational investigation, based on DFT calculations, of the structure, stability, and electronic properties of the Cu–Sn clusters $Cu_{4-n}Sn_n$ (n = 1–4) and compare their results to monometallic Cu_4 and Sn_4 systems. We considered a detailed characterization of the adsorption and activation (geometry changes, charge transfer) of CO_2 on the most stable structure of the monometallic and bimetallic Cu–Sn clusters and their efficacy towards the direct gas-phase dissociation of CO_2 to CO and O fragments. We then compare the free energy profiles for the eCO_2R to HCOOH and CO on isolated $Cu_{4-n}Sn_n$ (n = 1–4) clusters as well as on clusters supported on graphene ($Cu_{4-n}Sn_n$/graphene) and on the partially hydroxylated (110) surface of γ-Al_2O_3 ($Cu_{4-n}Sn_n$/γ-Al_2O_3). Finally, the free energies of the competitive HER on $Cu_{4-n}Sn_n$, $Cu_{4-n}Sn_n$/graphene and $Cu_{4-n}Sn_n$/γ-Al_2O_3 were also computed, from which we could conclude on the effect of composition and support on the selectivity towards CO or HCOOH.

2. Computational details

2.1 Computational methods

All DFT calculations were conducted with the "Vienna ab initio simulation package" (VASP, version 6.3.0)[30] together with the Perdew–Burke–Ernzerhof (PBE) exchange correlation functional[31] and the dispersion correction (Grimme's-D3).[32,33] A single (1 × 1 × 1) k-point and a (3 × 3 × 1) mesh were used for the nanoclusters and surface models, respectively, to sample the Brillouin zone of the simulation supercell. A plane-wave basis set within the framework of the projector augmented wave method[33] was used with a kinetic energy cutoff set to 450 eV. The transition state structures connecting adsorbed CO_2^* and $CO^* + O^*$ were determined using the climbing image nudged elastic band (cNEB) as implemented in VASP.[33,34] The eCO_2R to HCOOH and CO includes two concerted proton–electron transfer (CPET) steps. For example, the CPET steps leading to CO formation are (i) $CO_2^* + (H^+ + e^-) \rightarrow COOH^*$ and (ii) $COOH^* + (H^+ + e^-) \rightarrow CO + H_2O$.[35] The competitive HER to generate H_2 involves a single CPET step: $H^+ + e^- \rightarrow 1/2\ H_2$. The reaction free energies of these CPET steps were calculated using the computational hydrogen electrode (CHE) approach:[36]

$$\Delta G = \Delta E_{DFT} + \Delta E_{ZPE} - T\Delta S + \Delta G_{pH} + \Delta G_U \qquad (1)$$

The terms in eqn (1) are the reaction energy, ΔE_{DFT}, computed at the DFT-PBE level including the effect of hydration obtained with the VASPsol implicit solvation model;[37,38] the change of

13430 | Phys. Chem. Chem. Phys., 2023, 25, 13429–13441

This journal is © the Owner Societies 2023

zero point energy (ΔE_{ZPE}); the entropy change, ΔS, and the temperature, T, of the system set at 298.15 K; the free energy correction due to the difference in proton concentration, $\Delta G_{pH} = 2.303 \cdot k_B \cdot T \cdot pH$ (pH = 0 as assumed in this paper); and the free energy correction due to the difference in electrode potential, $\Delta G_U = -neU$, where n is the number of electrons transferred, e is the electronic charge, and U is the applied potential ($U = 0$ as assumed in this paper). The zero-point energies and entropies were determined within the harmonic approximation by taking the vibrational frequencies of adsorbates and molecules calculated with DFT. Based on previous studies using the CHE model,[39] the variations in E_{ZPE} and S were considered to be small compared to variations in the reaction energies based on E_{DFT} alone and, therefore, to be constant for all systems in this study.

2.2 Computational models

The structures of Cu–Sn nanocluster models were identified using the *ab initio* random structure searching (AIRSS) code,[40] an unbiased approach that has been used extensively to predict the structure of a variety of materials, including clusters.[41,42] The starting point for each calculation is a set of atoms corresponding to the monometallic, (Cu$_4$) and (Sn$_4$), and bimetallic, Cu$_{4-n}$Sn$_n$ (n = 1–3), clusters placed randomly within the central volume of a large cube of edge length 20 Å to minimize the interactions between the periodic images. For each system, we generated fifty random structures. The efficiency of the searches was improved by employing constraints on the minimum interatomic separations of the initial structure: d(Cu–Cu) = 2.1 Å and d(Sn–Sn) = 2.6 Å.[42] The energies of the atomic structures generated by AIRSS were determined with VASP. From the DFT energies of the random structure, the Boltzmann factor f_i corresponding to each ith isomer was evaluated according to the expression

$$f_i = \frac{e^{-(E_i - E_0)/RT}}{\sum_j e^{-(E_j - E_0)/RT}} \qquad (2)$$

where E_i is the energy of the ith candidate structure and E_0 is the energy of the most stable candidate structure. We selected the candidates with a Boltzmann factor $f_i \geq 0.01$ and, to increase our sampling, we also considered ten to fifteen randomly selected structures such that $1 \leq E_i - E_0 \leq 3$ eV. These structures were subject to geometry optimization to determine the most stable Cu, Sn and Cu–Sn clusters. During structural relaxation, we used a convergence criterion of 10^{-6} eV for the energy change and 0.01 eV Å^{-1} for the forces. The structures of the most stable clusters were supported on graphene and on the (110) surface of γ-Al$_2$O$_3$. The coordinates of γ-Al$_2$O$_3$ ($P2_1/m$ space group)[43] were used as the starting geometry to optimize the internal coordinates and cell parameters of the bulk structure of γ-Al$_2$O$_3$.[44] The values of the optimized lattice parameters of γ-Al$_2$O$_3$ were a = 5.538 Å, b = 8.347 Å, c = 8.024 Å, β = 90.6° and $\alpha = \gamma$ = 90.0°. Starting from the optimized bulk structure, we generated a 2 × 2 × 1 supercell of partially hydroxylated slabs of the γ-Al$_2$O$_3$ (110) surface containing three atomic layers. In fact,

previous IR experiments showed that isolated hydroxyl (OH) groups (around 3701 cm^{-1}) at the γ-Al$_2$O$_3$ surfaces were present even after annealing at 900 °C for 30 min.[45] The lattice parameters of the unit cell were 16.05 Å and 10.02 Å and the vacuum space in the z-direction was set to 21.71 Å. All atoms were relaxed during the optimization. For graphene-supported nanoclusters, a 5 × 5 × 1 supercell was used. Calculation of the energy of adsorption of the Cu$_{4-n}$Sn$_n$ (n = 0–4) clusters on the graphene and γ-Al$_2$O$_3$ (100) surfaces shows a favorable interaction between the Cu–Sn clusters and the support (Table S2 in the ESI†). The adsorption and dissociation of CO$_2$ were studied using the most stable structure of every composition of the Cu$_{4-n}$Sn$_n$ (n = 1–4) clusters. To compute the free energy pathways for the electrochemical conversion of CO$_2$ to formic acid (CO$_2$ + 2H$^+$ + 2e$^-$ → HCOOH) and carbon monoxide (CO$_2$ + 2H$^+$ + 2e$^-$ → CO + H$_2$O), we started from the most stable optimized structure of adsorbed CO$_2$* and from it generated and optimised the structure of OCHO*, COOH* and CO* on the nanoclusters. The structures of all atomistic models generated in this study are provided in Section S2 of the ESI.†

3. Results and discussion

3.1 Structure, stability, and electronic properties of Cu–Sn clusters

The structures and relative energies of the low energy isomers of the tetrahedral Cu$_{4-n}$Sn$_n$ (n = 0–4) clusters are reported in Fig. 1. Since the thermal energy is $k_B T$ = 0.025 eV at T = 298.15 K, where k_B is the Boltzmann constant, we expect that for each cluster more than one isomer may coexist at room temperature if their energies are within the 0.25 eV energy range. According to Fig. 1, except for Cu$_3$Sn, the other bimetallic Cu–Sn clusters and pure Cu$_4$ and Sn$_4$ exist as one isomer at room temperature because the energy difference between the most stable isomer and its next higher energy isomer is more than 0.25 eV. The ground state of Cu$_4$ is a two-dimensional structure with D_{2h} symmetry, in agreement with previous studies (Fig. 1a).[7,20,46] The next higher energy isomer of Cu$_4$ is also a 2D structure with a planar-triangular geometry and C_s symmetry, which is 0.4 eV higher in energy than the lowest energy isomer. The bimetallic Cu$_3$Sn cluster has three isomers with similar energy: the most stable is a distorted three-dimensional (3D) structure with C_s symmetry, followed by an isomer of tetrahedral geometry (0.06 eV), and an isomer where the planarity of the Cu$_4$ cluster is preserved (C_{2v} symmetry, 0.17 eV) (Fig. 1b). For Cu$_2$Sn$_2$, the distorted 3D (C_{2v}) and tetrahedral (D_{2h}) structures were found to be the most stable isomers but in this bimetallic cluster the energy difference between them is large (0.83 eV) (Fig. 1c). For CuSn$_3$, the ground-state 2D structure with the Sn atoms forms trigonal geometry with the Cu atom at the lateral position, the second most stable isomer is a 3D pyramidal structure, and the least stable one has a 2D rhombus-like geometry (Fig. 1d). Like Cu$_4$, the most stable isomer of the Sn$_4$ cluster has a two-dimensional structure with D_{2h} symmetry (Fig. 1e). Overall, the four atom clusters of the ground-states of monometallic Cu$_4$
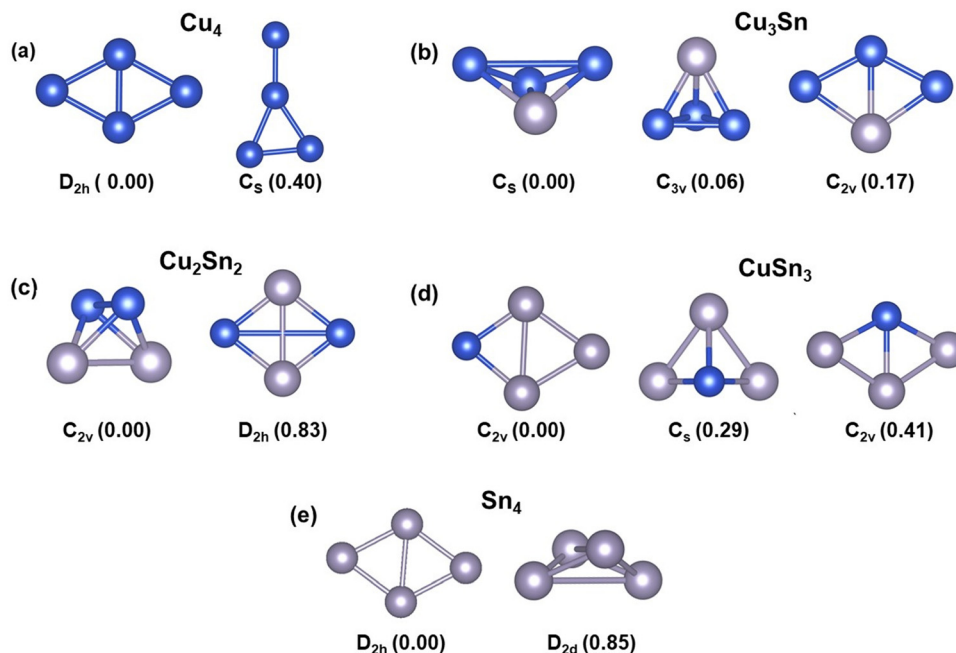
This journal is © the Owner Societies 2023

Phys. Chem. Chem. Phys., 2023, **25**, 13429–13441 | **13431**

Fig. 1 The lowest energy isomers of the four-atom $Cu_{4-n}Sn_n$ ($n = 0-4$) clusters: (a) Cu_4; (b) Cu_3Sn; (c) Cu_2Sn_2; (d) $CuSn_3$; (e) Sn_4. The symmetry of the structures is given at the bottom of each isomer. The values within the parenthesis are the relative energies (in eV) of the cluster relative to the most stable isomer. Blue and grey balls represent Cu and Sn atoms, respectively.

and Sn_4 have a 2D planar rhombus-like geometry, whereas the mixed Cu–Sn clusters tend to form distorted 3D, tetrahedral, and quasi-planar geometries.

To gain insights into the relative stabilities of pure and bimetallic four-atom systems, we computed the binding energy per atom (E_B), here defined as

$$E_B = -\frac{E(Cu_{4-n}Sn_n) - (4-n)E(Cu) - nE(Sn)}{4} \qquad (3)$$

where $E(Cu_{4-n}Sn_n)$ is the total energy of the most stable isomer of each $Cu_{4-n}Sn_n$ ($n = 0-4$) cluster, and $E(Cu)$ and $E(Sn)$ are the total energies of Cu and Sn atoms, respectively. A higher positive value of E_B indicates higher thermodynamic stability of the cluster. As the variation of binding energy does not always provide a clear picture of the relative stability of the

nanoclusters, we have also employed the second-order difference in energy (Δ_2E):

$$\Delta_2E(Cu_nSn_m) = E(Cu_{n+1}Sn_{m-1}) + E(Cu_{n-1}Sn_{m+1}) - 2(Cu_nSn_m) \qquad (4)$$

The Δ_2E index assesses the stability of a cluster, Cu_nSn_m, compared with its neighboring structures, $Cu_{n+1}Sn_{m-1}$ and $Cu_{n-1}Sn_{m+1}$. A higher value of Δ_2E signifies a greater stability for the cluster as compared to its nearest neighbors. Table 1 reports the values of the energy descriptors E_B and Δ_2E together with a list of electronic properties of the clusters: the energy difference between the highest occupied molecular orbital (HOMO) and the lowest unoccupied molecular orbital (LUMO) (HOMO–LUMO gap, Δ_{H-L}), the Bader charges (Q_B) of the Cu and Sn atoms, and the average interatomic distance between nearest neighbors. According to Table 1, the two isomers of Cu_4

Table 1 Binding energy per atom (E_B), second-order energy difference (Δ_2E), HOMO–LUMO gap (Δ_{H-L}), Bader charge (Q_B), and average distance (d) between atoms

System	Symmetry	E_B (eV)	Δ_2E (eV)	Δ_{H-L} (eV)	Q_B(Cu) (e)	Q_B(Sn) (e)	d_{Cu-Cu} (Å)	d_{Cu-Sn} (Å)	d_{Sn-Sn} (Å)
Cu_4	D_{2h}	1.42	—	0.94	—	—	2.34	—	—
	C_s	1.32	—	0.96	—	—	2.32	—	—
Cu_3Sn_1	C_s	1.68	0.08	1.33	−0.67	2.01	2.8	2.53	—
	C_{3v}	1.66	—	1.71	−0.64	1.91	2.43	2.53	—
	C_{2v}	1.64	—	1.67	−0.61	1.84	2.33	2.54	—
Cu_2Sn_2	C_{2v}	1.92	1.01	0.97	−0.92	0.92	2.49	2.6	2.88
	D_{2h}	1.71	—	0.91	−1.68	1.68	3.94	2.52	3.14
Cu_1Sn_3	C_s	1.91	−0.97	1.94	−1.81	0.60	—	2.53	2.84
	C_s	1.84	—	1.29	−1.38	0.46	—	2.63	3.04
	C_{2v}	1.81	—	1.33	−0.69	0.23	—	2.62	2.78
Sn_4	D_{2h}	2.14	—	1.03	—	—	—	—	2.92
	D_{2d}	1.93	—	1.62	—	—	—	—	3.27

have the lowest binding energies (1.42 eV for D_{2h} and 1.32 eV for C_s) out of all four-atom clusters. The value of E_B increases with the incorporation of more Sn atoms, with the maximum value (2.14 eV) computed for the monometallic Sn_4 cluster. Assessing from the binding energies, the stability of the four-atom bimetallic $Cu_{4-n}Sn_n$ is more than that of pure Cu_4 and it is the highest for Cu_2Sn_2 (1.92 eV). From the results of second-order difference in the energy, $\Delta_2 E$, we observe that among the three bimetallic Cu–Sn clusters considered here, the lowest energy isomer of Cu_2Sn_2 exhibits greater stability than the respective isomers of Cu_3Sn and $CuSn_3$. In summary, the Cu_4 cluster is thermodynamically the least stable. However, the cluster stability is strongly affected by its composition: the incorporation of Sn stabilizes the Cu–Sn system compared to the pure copper cluster.

From Table 1, the stability correlates with the average interatomic distances in the cluster. The average Cu–Cu distance of the lowest energy isomer is 2.34 Å, in good agreement with other DFT plane wave studies of Cu clusters (2.36 Å).[47] This average interatomic distance increases to 2.92 Å in Sn_4 because of the different atomic radii of Cu (1.28 Å) and Sn (1.41 Å). In the bimetallic clusters, the trend is an increase of Cu–Cu and a decrease of Sn–Sn, while Cu–Sn distances lie between the Cu–Cu and Sn–Sn distances. We also conducted a Bader charge (Q_B) analysis to determine the charge distribution in the Cu–Sn clusters.[48–50] In Cu_3Sn, Cu_2Sn_2 and $CuSn_3$, the copper and tin atoms have negative and positive Bader charges, respectively (see Table 1). Consequently, during the reduction reaction, the electron transfer process will occur from the electron-rich Cu atoms to the C atom of CO_2, which is in its highest oxidation state. A descriptor to analyze the global reactivity is the gap energy, Δ_{H-L}. This property relates to the energy cost for an electron to jump from the HOMO to the LUMO orbital and, therefore, characterizes the chemical stability of the system, with a higher value of Δ_{H-L} corresponding to a more chemically stable (less reactive) cluster. If we compare the values of Δ_{H-L} of the most stable isomers of each monometallic and bimetallic cluster, Cu_4 has the lowest HOMO–LUMO gap (0.94 eV). This value increases substantially for Cu_3Sn (1.33 eV) and $CuSn_3$ (1.94 eV) but is similar in Cu_2Sn_2 (0.97 eV). In summary, from the energy descriptors E_B and $\Delta_2 E$ and the electronic descriptor Δ_{H-L}, Cu_2Sn_2 is the most stable cluster and maintains the reactivity of the pure copper cluster.

3.2 The adsorption and activation of CO_2

The activation of CO_2 is a result of the electronic charge transfer from the HOMO of the cluster to the LUMO of the CO_2 molecule.[51] To investigate the direction of charge migration between the clusters and CO_2, we have compared in Fig. 2 the energies of the HOMO and LUMO of the most stable isomers of Cu–Sn with those of gas-phase CO_2. For all clusters, the energy difference between the HOMO of CO_2 and the LUMO of the clusters (dark gray dashed line) is higher than the energy difference between the HOMO of the clusters and the LUMO of CO_2 (blue dashed line). For example, the energy difference between the HOMO of Cu_4 and the LUMO of CO_2 is 3.38 eV,
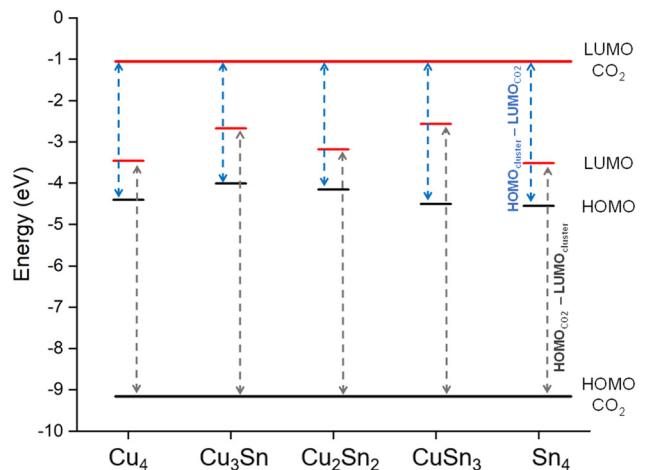

Fig. 2 The HOMO (black line) and LUMO (red line) energy levels of monometallic and bimetallic tetrahedral Cu–Sn clusters compared to that of CO_2. The dark grey dashed line represents the energy difference between the HOMO of CO_2 and the LUMO of the clusters. The blue dashed line is the energy difference between the HOMO of the clusters and the LUMO of CO_2.

while the energy difference between the HOMO of CO_2 and the LUMO of Cu_4 is 5.68 eV. Similarly, the energy difference between the HOMO of monometallic Sn_4 and the LUMO of CO_2 is 3.52 eV, while the energy difference between the HOMO of CO_2 and the LUMO of monometallic Sn_4 is 5.62 eV. The charge migration from clusters to the CO_2 molecule is favorable, which results in radical anion $CO_2^{-\delta}$ formation upon CO_2 adsorption.

The first step in the catalytic conversion of CO_2 is the adsorption process, in which the molecule can physisorb or chemisorb to the catalyst. In the physisorbed state, the CO_2 molecule maintains the C–O bond length (1.18 Å) and the O–C–O bond angle ($180°$) of the gas phase molecule. In contrast, in the chemisorbed state, the CO_2 molecule shows elongated C–O bonds and a decreased O=C=O bond angle (linear to bent mode), which corresponds to the activation of CO_2 because of the charge transferred from the metal catalyst to the π^* molecular orbitals of the CO_2 molecule.[52] Fig. 3 displays the physisorption and chemisorption of CO_2 on monometallic and bimetallic four-atom $Cu_{4-n}Sn_n$ ($n = 0–4$) clusters. When physisorbed, CO_2 prefers "top" coordination with the O interacting with the Cu atom. When chemisorbed, CO_2 coordinates at the bridge site between the electron-rich Cu and the electron-deficient Sn (Table 1) leading to the formation of Cu–C and Sn–O bonds. From Fig. 3, we also note that on the pure tin cluster, Sn_4, we could only locate a weakly physisorbed CO_2 state. We have further characterised in Table 2 the interaction and activation of CO_2 on the $Cu_{4-n}Sn_n$ ($n = 0–4$) clusters relative to the properties of the CO_2 molecule in gas phase using the following energetic, structural, and electronic indicators: adsorption energy (ΔE_{CO_2}); C–O elongation (d_{C-O}); O–C–O angle bending (θ_{OCO}); and charge transfer from the cluster to CO_2 (ΔQ). The adsorption energy (ΔE_{CO_2}) was computed according to the following expression:

$$\Delta E_{CO_2} = E[(Cu_{4-n}Sn_n)\cdots CO_2] - E(CO_2) - E(Cu_{4-n}Sn_n) \quad (5)$$
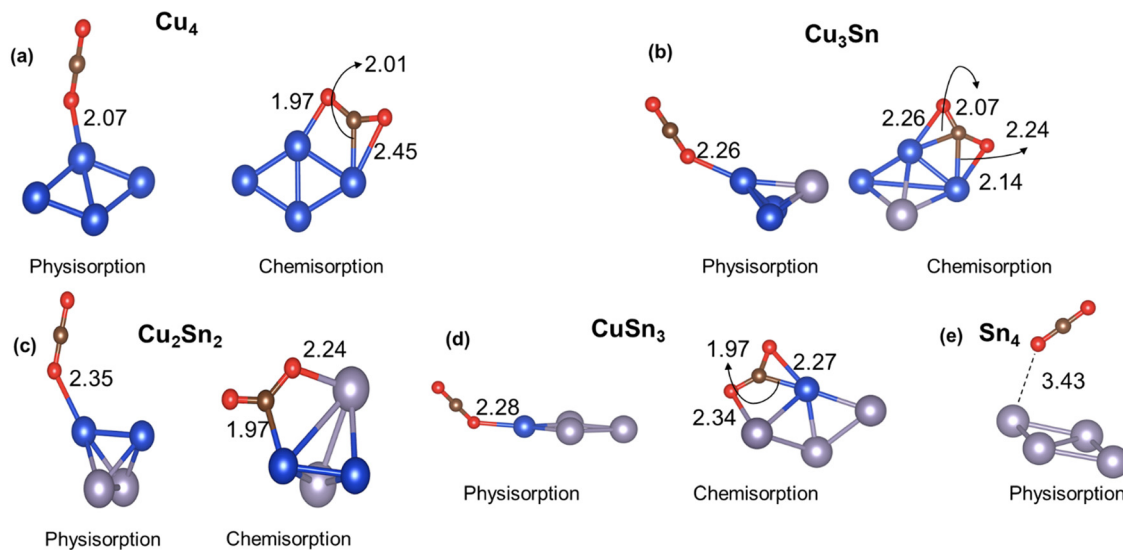
This journal is © the Owner Societies 2023

Phys. Chem. Chem. Phys., 2023, **25**, 13429–13441 | **13433**

Fig. 3 Lowest energy structures of CO_2 physisorbed and chemisorbed on monometallic and bimetallic Cu–Sn clusters. Blue, grey, brown, and red balls represent Cu, Sn, C and O atoms, respectively.

Table 2 Adsorption energy (ΔE_{CO_2}), C–O bond length ($d_{C–O}$), and bond angle (θ_{OCO}) of CO_2, and charge transfer from the catalyst to CO_2 using Bader analysis (ΔQ) when physisorbed and chemisorbed on the $Cu_{4-n}Sn_n$ (n = 0–4) clusters. For comparison, the bond length and the bond angle of the CO_2 molecule in the gas phase are 1.18 Å and 180 degrees, respectively

System	Physisorption				Chemisorption			
	ΔE_{CO_2} (eV)	$d_{C–O}$ (Å)	θ_{OCO} (°)	ΔQ (e)	ΔE_{CO_2} (eV)	$d_{C–O}$ (Å)	θ_{OCO} (°)	ΔQ (e)
Cu_4	−0.32	1.18, 1.17	179.7	−0.01	−0.53	1.26, 1.22	140	−0.51
Cu_3Sn	−0.32	1.18,1.17	179.5	−0.03	−0.21	1.23,1.24	142.6	−0.52
Cu_2Sn_2	−0.14	1.18, 1.17	179.3	−0.02	0.50	1.28, 1.22	132.7	−0.64
$CuSn_3$	−0.18	1.19, 1.17	179.6	−0.01	0.40	1.24, 1.27	136.9	−0.70
Sn_4	−0.16	1.18, 1.80	179.9	0.00	—	—	—	—

where the first term is the energy of the cluster–CO_2 complex, and the second and third terms are the energies of the isolated CO_2 molecule and the pristine cluster, respectively. Here, a negative value of the adsorption energy indicates a favorable interaction between CO_2 and the metal cluster.

The results in Table 2 confirm that when CO_2 chemisorbs to the cluster, there is a significant elongation of the C–O bond, loss of linearity of CO_2, and charge transfer, which does not occur when CO_2 is physisorbed. For the chemisorbed state, the inclusion of Sn leads to a more pronounced bending of the CO_2 molecule (140.0° for Cu, 142.6° for Cu_3Sn, 132.7° for Cu_2Sn_2, and 136.9° for Cu_3Sn) and charge transfer compared to pure Cu (−0.51e for Cu_4, −0.52 for Cu_3Sn, −0.64e for Cu_2Sn_2, and −0.70e for $CuSn_3$). However, there is a counterintuitive behaviour in the inverse relationship between the charge transferred to CO_2 and the adsorption energy: a higher charge transfer from the Cu–Sn cluster to CO_2 does not correspond to a favourable adsorption energy. As shown in Table 2, the interaction of CO_2 on Cu_4 and Cu_3Sn is favourable for both chemisorption and physisorption (ΔE_{CO_2} < 0 in Table 2). On the other hand, for the other Cu–Sn clusters, the CO_2 chemisorption (ΔE_{CO_2} > 0) is less stable than physisorption (ΔE_{CO_2} < 0). The higher activation of CO_2 in Sn-bearing clusters (charge transfer

and bending) does not correspond to a favourable interaction between the CO_2 and the catalyst, as previously shown in tetrahedral Cu–Pd, Cu–Ni, and Cu–Zr clusters.[20,21] For the Cu_3Sn system, we have considered the CO_2 adsorption on the three low-energy isomers in Fig. 1(b) because their energy difference is less than 0.2 eV but, upon optimization, the C_{2v} and C_{3v} isomers of Cu_3Sn rearranged to the C_s isomer (see Fig. S5 in the ESI†). The structures of the $Cu_3Sn\cdots CO_2$ complex in Fig. 2(b) and the values in Table 2 refer to the lowest energy adsorption site of CO_2. In comparison, previous DFT calculations of CO_2 adsorption on other four-atom Cu clusters doped with Pd, Ni, Pt and Zr reported values of ΔE_{CO_2} (up to −1 eV) corresponding to more favorable adsorption and Bader charge transfer (up to 1e) compared to the Cu–Sn clusters (Table S3 of the ESI†).[18–20] CO_2 is adsorbed weakly on the Cu–Sn clusters compared to Cu–Pd, Cu–Ni, Cu–Pt and Cu–Zr. However, the values of θ_{OCO} and d_{CO} are close to those found for Cu–Pd, Cu–Ni, Cu–Pt and Cu–Zr (Table S3, ESI†). Therefore, adsorption energy is not always a good indicator of CO_2 activation.

The adsorption energy, bond length, bond angle, and the overall charge of the CO_2 molecule physisorbed on graphene and γ-Al_2O_3 supported $Cu_{4-n}Sn_n$ (n = 0–4) clusters are reported in Table S4 of the ESI.† For most clusters on graphene and

γ-Al_2O_3, the physisorption of CO_2 has favourable adsorption energy with a small charge transfer, between $-0.01e$ and $-0.03e$, to the CO_2 molecule. However, for $CuSn_3$/graphene and Cu_3Sn/γ-Al_2O_3, CO_2 is in the chemisorbed state, as shown by the significant bending of CO_2 and elongation of C–O (Fig. S3 and S4 of the ESI†). The Bader charge transfer for the chemisorbed CO_2 is between -1.0 and $-1.6e$, much higher than that for the unsupported clusters reported in Table 2 (-0.5 to $-0.7e$). However, the chemisorption of CO_2 is not favorable in $CuSn_3$/graphene, as evidenced by the positive adsorption energy of 0.34 eV. Similarly, for Cu_3Sn/γ-Al_2O_3, the chemisorption of CO_2 seems to be favorable with a high Bader charge transferred to CO_2.

3.3 CO_2 direct dissociation over $Cu_{4-n}Sn_n$ clusters

The favorable chemisorption on monometallic Cu_4 compared to Cu–Sn clusters motivated us to determine if the activation of CO_2 (chemisorption) affects the kinetic barrier for breaking the C–O bond. To model the gas-phase CO_2 dissociation on the $Cu_{4-n}Sn_n$ ($n = 0$–4) clusters we used the following reaction: $CO_2^* \rightarrow CO^* + O^*$. To this end, we performed transition state search calculations to find the energy barrier to break one of the C–O bonds of the CO_2 molecule. The starting point was the most stable structure of adsorbed CO_2. The final product was modelled by choosing the most elongated C–O bond of the adsorbed CO_2, systematically increasing the bond distance to nearly 3.0 Å and optimizing the resulting structure.[21] The relative energies of the reactant complexes (CO_2^*), transition state (TS) and product complexes ($CO^* + O^*$) are reported in Fig. 4 together with the structures of these intermediates for Cu_4. The optimized structures of the initial state, transition state, and final state involved in CO_2 direct dissociation to CO over the other clusters are reported in Fig. S1 of the ESI.† Activation barriers of forward ($E_{a,f}$) and backward ($E_{a,b}$) reactions, the reaction energy (ΔE) measuring the energy difference between the reactant (CO_2^*) and the product ($CO^* + O^*$), and

Table 3 Adsorption energy (E_A), forward ($E_{a,f}$) and backward ($E_{a,b}$) activation barriers, reaction energy (ΔE) of the CO_2 direct dissociation ($CO_2^* \rightarrow CO^* + O^*$), and C–O bond distance (d_{CO}) of the adsorbed CO fragment in the final dissociated product for CO_2 dissociation over $Cu_{4-n}Sn_n$ ($n = 0$–4)

System	E_A (eV)	$E_{a,f}$ (eV)	$E_{a,b}$ (eV)	ΔE (eV)	d_{CO} (Å)
Cu_4	-0.53	2.30	2.30	0.00	1.16
Cu_3Sn_1	-0.32	2.30	2.09	0.21	1.16
Cu_2Sn_2	-0.14	3.14	2.32	0.82	1.15
Cu_1Sn_3	-0.18	2.18	2.10	0.08	1.15

the C–O bond distance of the adsorbed CO fragment in the final dissociated product (d_{CO}) are summarized in Table 3. The energy barrier to dissociate adsorbed CO_2 and form the CO^* and O^* products is between 2.2 and 3.1 eV. Specifically, the activation energy for the dissociation of CO_2 on Cu_4 is 2.3 eV, which is close to the value of 2.4 eV obtained by Mondal and co-workers using the B3LYP functional with the Stuttgart pseudo-potential basis set (SDD) for Cu and the triple-zeta basis set for C and O.[21] However, another DFT study using the PBE0 functional with the SDD basis set for all atoms gave a much lower barrier of 1.8 eV.[20] The double zeta basis set in these calculations could cause such discrepancy, not observed in our case because of the use in this study of delocalized plane waves to describe all atoms. As the reaction energy over Cu_4 is close to zero, the direct gas-phase CO_2 dissociation could thermodynamically occur on this cluster, but the process is kinetically limited. The results in Table 3 also suggest that except for Cu_2Sn_2, the energetics of the CO_2 direct dissociation reaction are not significantly affected by the incorporation of Sn. The activation barrier for Cu_3Sn is similar to that of monometallic Cu_4 (see Fig. 4). It is the highest for Cu_2Sn_2 (3.1 eV), and the lowest for $CuSn_3$ (2.18 eV). The formation of Cu–Sn bonds does not lower the activation energy compared to the monometallic clusters, leading to values for the kinetic barriers close to that found for Cu_4, suggesting a lack of synergy between copper and tin atoms to modulate activation barriers of the gas-phase CO_2 direct dissociation. In comparison, other reports of four-atom copper-based clusters showed modulation of the activation barriers (higher or lower values of ΔE and $E_{a,f}$) depending on the cluster composition. For Cu–Zr, the activation barrier was found to be between 0.13 and 0.52 eV, with Cu_3Zr having the lowest activation energy but also strong adsorption (-3.1 eV) of the final product (*CO and O^*), which could lead to poisoning of the catalyst surface.[21] The CO_2 direct dissociation on Cu–Pd clusters had an activation barrier of 1.1 to 2.8 eV, values which are generally lower than those for Cu–Sn (Table 3). The activation barriers of the direct CO_2 dissociation on the Cu–Sn clusters are also higher than those reported for four-atom Pt–Ni clusters.[53]

The adsorption energy of CO_2 on these clusters is significantly lower than the dissociation barrier for the cleavage of the C–O bond, suggesting that the adsorption of CO_2 will be more favorable than the direct dissociation of CO_2. The positive values of the reaction energy ΔE, which is the energy difference between the reaction and the final products, suggest that for Cu_2Sn_2 and Cu_3Sn, the dissociation of CO_2 to CO + O is
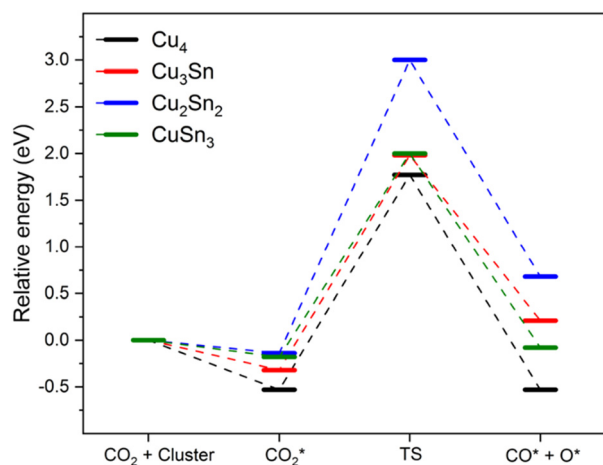

Fig. 4 Reaction pathway for CO_2 dissociation into CO^* and O^* over Cu_4, Cu_3Sn, Cu_2Sn_2, and $CuSn_3$ clusters. The structures are those of the chemisorbed CO_2, transition state, and ($CO^* + O^*$) on Cu_4. Blue, brown, and red balls represent metal Cu, C and O atoms, respectively.
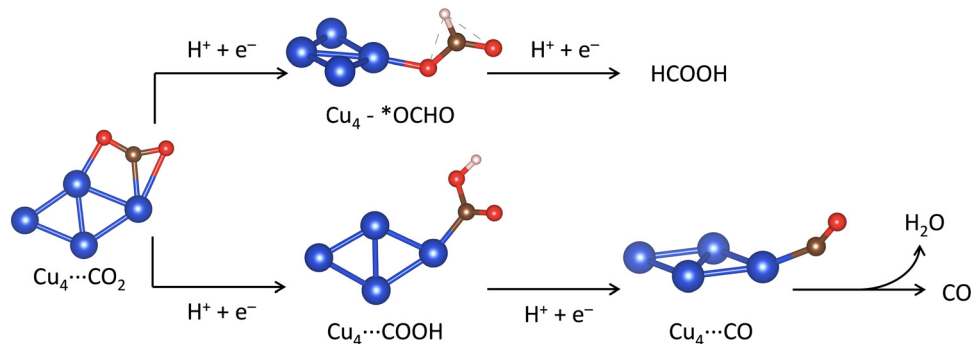
This journal is © the Owner Societies 2023

Phys. Chem. Chem. Phys., 2023, **25**, 13429–13441 | **13435**

Fig. 5 Reaction pathways for the two proton/two electron (2H⁺/2e⁻) CO₂ reduction reaction to carbon monoxide (CO) and formic acid (HCOOH) showing the optimised structures of the intermediates on Cu₄. Blue, brown, red and white balls represent metal Cu, C, O and H atoms, respectively.

endothermic. The highly positive ΔE of 0.82 for Cu_2Sn_2 compared to other clusters indicates that this would have an unstable final product. In summary, the gas-phase CO_2 direct dissociation, $CO_2^* \rightarrow CO^* + O^*$, is kinetically and thermodynamically unfavourable on Cu–Sn clusters and unlikely to occur.

3.4 Mechanisms of reduction reactions on Cu–Sn clusters

3.4.1 Electrochemical CO₂ reduction to carbon monoxide and formic acid. In this section, we present calculations of the mechanism of the electrochemical CO_2 reduction (eCO_2R) to CO and HCOOH catalyzed by the $Cu_{4-n}Sn_n$ clusters. We have also considered the effects of two supports, graphene and partially hydroxylated γ-Al₂O₃ (110) surface. The concerted proton–electron transfer (CPET) steps controlling the eCO_2R to HCOOH and CO are shown in Fig. 5. After the adsorption of CO_2^* to the catalyst surface, the first CPET step leads to two possible intermediates, OCHO* or COOH*, depending on the atom coordinated to the catalyst: O or C. The second CPET will then form HCOOH or CO accordingly. We have computed the free energy of reactions (ΔG) of the elementary steps leading to the formation of HCOOH and CO. For HCOOH, these steps are the CPET to convert adsorbed CO_2^* to an O-coordinated intermediate ($CO_2^* + H^+ + e^- \rightarrow OCHO^*$, ΔG_{OCHO^*}) and the next CPET converts adsorbed *OCHO to gas phase formic acid ($OCHO^* + H^+ + e^- \rightarrow HCOOH$, ΔG_{HCOOH}). For CO, the elementary steps are the CPET to convert adsorbed CO_2^* to a C-coordinated intermediate ($CO_2^* + H^+ + e^- \rightarrow COOH^*$, ΔG_{COOH^*}), and the next CPET converts adsorbed *COOH to adsorbed carbon monoxide ($COOH^* + H^+ + e^- \rightarrow CO^* + H_2O$, ΔG_{CO^*}), which can then be released from the catalyst surface to form gas-phase CO (ΔG_{CO}).

The Gibbs free energy diagrams of the eCO_2R reaction on the $Cu_{4-n}Sn_n$ (n = 0–4) clusters in Fig. 6(a–d) show that the CPET steps controlling the distribution of the HCOOH and CO products are significantly affected by the cluster composition and the type of support. Graphene-supported Cu–Sn clusters give lower energetic pathways for CO and HCOOH compared to γ-Al₂O₃. The optimized structures of the intermediates involved in the eCO_2R on the isolated and supported Cu₄ clusters are shown in Fig. 7. The Gibbs free energy diagram for the eCO_2R

pathways to HCOOH and CO on each Cu–Sn cluster is discussed in detail below. The optimized structures of the intermediates CO₂*, OCHO*, COOH*, and CO* adsorbed on Cu₄, Cu₄/graphene, and Cu₄/γ-Al₂O₃ are shown in Fig. 7. The intermediates over the other Cu–Sn clusters are reported in Fig. S2 and S4 of the ESI.†

Cu₄. According to Fig. 6(a), the adsorption of CO_2 is favorable on Cu₄ and Cu₄/graphene but not on Cu₄/γ-Al₂O₃ ($\Delta G_{CO_2^*}$ = 0.6 eV). On Cu₄, the eCO_2R is selective towards HCOOH because of the lower free energy of the *OCHO intermediate (ΔG_{OCHO^*} = 0.7 eV) compared to *COOH (ΔG_{COOH^*} = 1.0 eV). On Cu₄/γ-Al₂O₃, the intermediate OCHO* binds strongly to the catalyst (ΔG_{OCHO^*} = −1.8 eV) compared to COOH* (ΔG_{COOH^*} = −0.9 eV). Consequently, the subsequent CPET step favors CO formation as it is easier to release CO as a product from the catalyst than HCOOH. For Cu₄/graphene, the selectivity is towards CO formation as it is easier to form *COOH (ΔG_{COOH^*} = −0.4 eV) than *OCHO (ΔG_{OCHO^*} = 0.5 eV). In addition, the next CPET step from *COOH to *CO is also favorable (ΔG_{CO^*} = −0.2 eV). In summary, while the isolated Cu₄ is selective towards HCOOH, the effect of both graphene and γ-Al₂O₃ (110) is to drive the reaction towards CO formation. However, the strong binding of OCHO* on Cu₄/γ-Al₂O₃ could poison the eCO_2R on this catalyst.

Cu₃Sn. In Fig. 6(b), the CPET steps leading to the formation of *OCHO (ΔG_{OCHO^*} = −0.9 eV) and *COOH (ΔG_{COOH^*} = −0.9 eV) on the most stable isomer of Cu₃Sn (C_s) are both exergonic and the subsequent steps to generate HCOOH (ΔG_{HCOOH} = 1.4 eV) and CO (ΔG_{CO^*} = 1.1 eV) are highly endothermic. The Gibbs free energy diagrams for the other two isomers of Cu₃Sn are given in Fig. S6 (ESI†). On Cu₃Sn/γ-Al₂O₃, the strong binding of the *OCHO intermediate makes the formation of HCOOH (ΔG_{HCOOH} = 1.9 eV) highly unfavourable compared to *CO (ΔG_{CO^*} = 0.8 eV). The subsequent step to release CO is exergonic ($\Delta G_{CO(g)}$ = −0.5 eV). Unlike Cu₃Sn and Cu₃Sn/γ-Al₂O₃, on graphene the energetics for the reaction steps leading to HCOOH and CO are similar. The formation of *OCHO (ΔG_{OCHO^*} = 0.2 eV) is slightly favored compared to *COOH (ΔG_{COOH^*} = 0.3 eV). However, the next step from

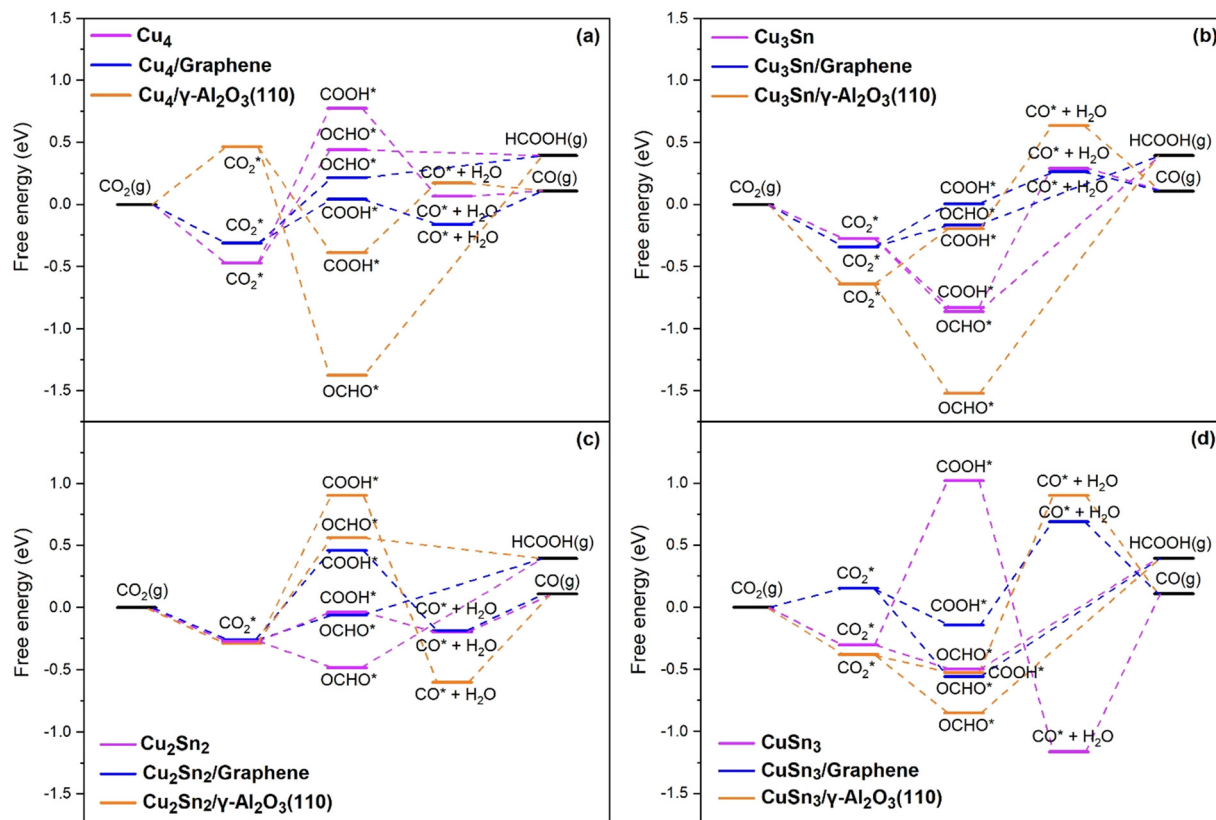**13436** | *Phys. Chem. Chem. Phys.*, 2023, **25**, 13429–13441

This journal is © the Owner Societies 2023

Fig. 6 Gibbs free energy diagram for the eCO$_2$R pathways to HCOO and CO on the (a) Cu$_4$, (b) Cu$_3$Sn, (c) Cu$_2$Sn$_2$, and (d) CuSn$_3$ clusters. Reduction pathways on isolated Cu$_{4-n}$Sn$_n$ (n = 1–3) clusters (light purple) and clusters supported on graphene (blue) and on the partially hydroxylated (110) surface of γ-Al$_2$O$_3$ (orange).

OCHO to HCOOH(g) has higher positive free energy ($\Delta G_{\text{HCOOH(g)}}$ = 0.6 eV) relative to the formation of CO ($\Delta G_{\text{CO*}}$ = 0.3 eV), whose desorption energy from the surface ($\Delta G_{\text{CO(g)}}$) is −0.2 eV.

Cu$_2$Sn$_2$. For the Cu$_2$Sn$_2$ system, the *OCHO intermediate ($\Delta G_{\text{OCHO*}}$ = −0.2 eV) is more stable than *COOH ($\Delta G_{\text{COOH*}}$ = 0.3 eV), but, overall, the energy pathway of CO formation ($\Delta G_{\text{CO*}}$ = −0.2 eV) is lower than that of HCOOH(g) formation ($\Delta G_{\text{HCOOH(g)}}$ = 0.8 eV). This Cu–Sn cluster is, therefore, selective towards CO. The support effect is destabilizing both *OCHO and *COOH intermediates. On Cu$_2$Sn$_2$/graphene, the *OCHO formation ($\Delta G_{\text{OCHO*}}$ = 0.2 eV) is more favorable than *COOH formation ($\Delta G_{\text{COOH*}}$ = 0.7 eV) and the overall selectivity is towards HCOOH compared to CO as it has the lowest energetic pathway. On the Cu$_2$Sn$_2$/γ-Al$_2$O$_3$ system, the first CPET steps to form COOH* ($\Delta G_{\text{COOH*}}$ = 1.2 eV) and OCHO* ($\Delta G_{\text{OCHO*}}$ = 0.8 eV) are both highly unfavorable. The overall product selectivity is towards HCOOH relative to CO, as evidenced by the overpotential for HCOOH (0.44 eV) being less than that for CO (1.07 eV) formation.

CuSn$_3$. For gas-phase CuSn$_3$, the electrochemical CO$_2$-to-CO conversion is highly unfavourable because of the strong CO* adsorption ($\Delta G_{\text{CO*}}$ = 2.2 eV). In comparison, the highest free energy of the reaction step for the HCOOH pathway is $\Delta G_{\text{HCOOH(g)}}$ = 0.9 eV. The CuSn$_3$ cluster is, therefore, selective towards the formation of HCOOH. In the Cu$_3$Sn/γ-Al$_2$O$_3$ system, the *OCHO formation ($\Delta G_{\text{OCHO*}}$ = −0.5 eV) is more favourable than COOH* formation ($\Delta G_{\text{COOH*}}$ = −0.1 eV). The subsequent steps from *COOH to *CO ($\Delta G_{\text{CO*}}$ = 1.4 eV) and from *OCHO to HCOOH (ΔG_{HCOOH} = 1.2 eV) are unfavourable. The HCOOH reaction pathway is lower compared to CO in this system. For the CuSn$_3$/graphene system, the *OCHO intermediate ($\Delta G_{\text{OCHO*}}$ = −0.7 eV) is more favourable than *COOH ($\Delta G_{\text{COOH*}}$ = −0.3 eV). The subsequent steps for both initial intermediates have a positive Gibbs free energy ($\Delta G_{\text{CO*}}$ = 0.8 eV and $\Delta G_{\text{HCOOH(g)}}$ = 1.0 eV). Moreover, the limiting potential for the electrochemical pathways shows CO (0.83 V) to be slightly lower than HCOOH (0.95 V).

The correlation of the Bader charge of Cu of supported clusters with the overpotential for the eCO$_2$R reactions to HCOOH and CO is reported in Fig. 8. For both reaction pathways, the greater the negative charge on Cu, the higher the overpotential. The only exceptions are Cu$_4$ and Cu$_3$Sn on γ-Al$_2$O$_3$. Since the site for CO$_2$ adsorption on the clusters is always the Cu atom (see Fig. S4, ESI†), a higher charge transferred to the Cu atoms will lead to stronger binding of the intermediates. However, there is a difference in the charge distribution on the catalyst depending on the support. For the
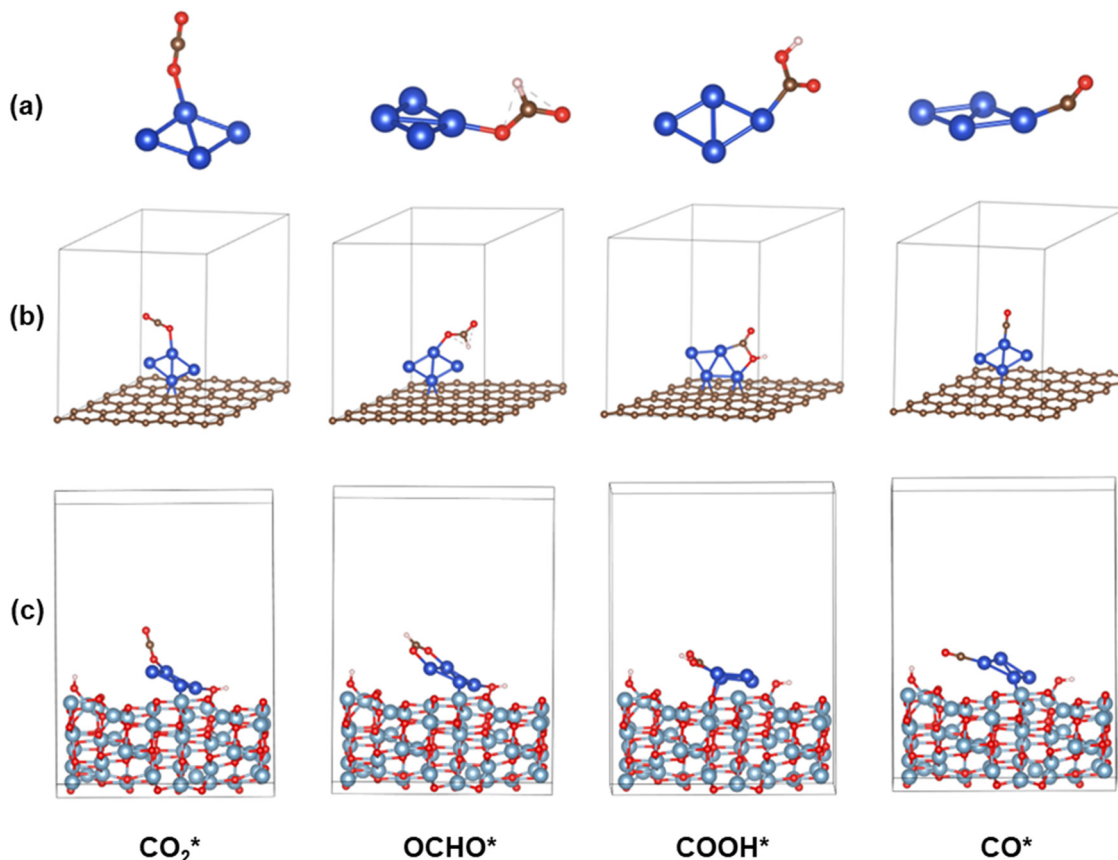
This journal is © the Owner Societies 2023

Phys. Chem. Chem. Phys., 2023, **25**, 13429–13441 | **13437**

Fig. 7 Optimized structures of the CO_2*, OCHO*, COOH*, and CO* intermediates on (a) Cu_4, (b) Cu_4/graphene, and (c) Cu_4/γ-Al_2O_3 (110). Blue, grey, brown, red and white balls represent Cu, Al, C, O and H atoms, respectively.
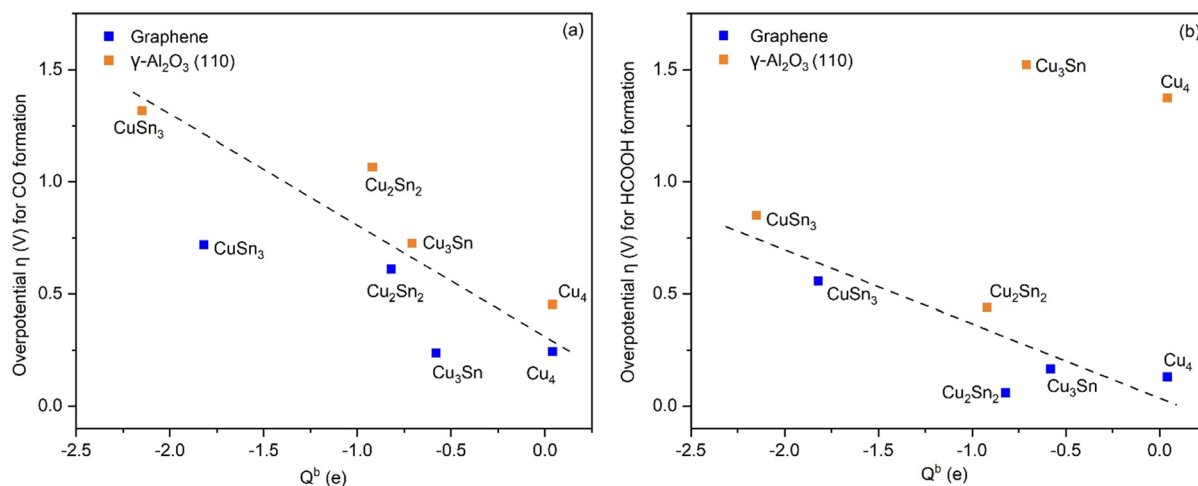

Fig. 8 Overpotential for CO and HCOOH formation as a function of the Bader charge, Q^b, of Cu in the Cu–Sn clusters supported on graphene (blue) and γ-Al_2O_3 (orange). The dashed black lines in both figures serve as a guide to the eye.

Cu–Sn clusters on γ-Al_2O_3, the Bader charge of Cu is higher compared to the case when the support is graphene. This behavior correlates with a higher overpotential for the reactions on Cu–Sn/γ-Al_2O_3 (*vide infra*). Overall, the cluster composition and support influence the reaction energetics and hence the final product selectivity. This shows the importance of tuning

the properties of the active sites to tune the binding of the intermediates to control the selective formation of a specific product.

3.4.2 Hydrogen evolution reduction. Since eCO$_2$R occurs in aqueous solutions, there is always a competition between CO$_2$R and HER ($H^+ + e^- \rightarrow 1/2\ H_2$). The faradaic efficiency of HER is

13438 | *Phys. Chem. Chem. Phys.*, 2023, **25**, 13429–13441
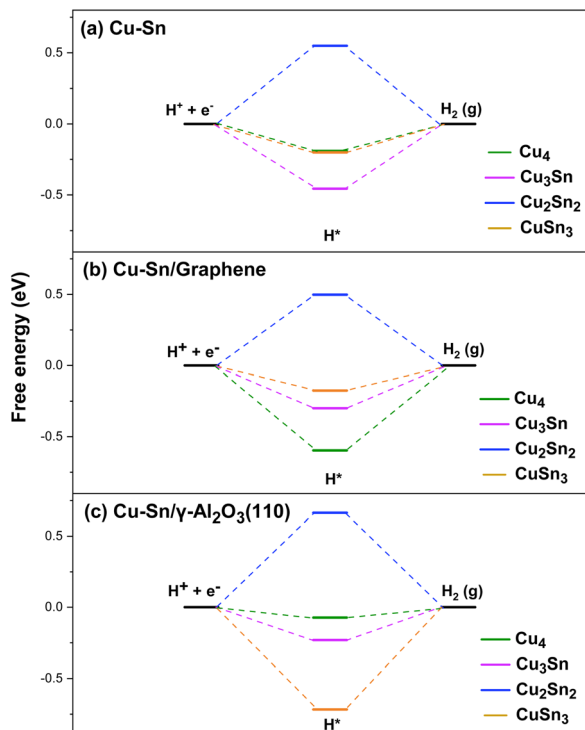
This journal is © the Owner Societies 2023

Fig. 9 Gibbs free energy diagram for the HER pathways to HCOO and CO on the (a) Cu_4, (b) Cu_3Sn, (c) Cu_2Sn_2, and (d) $CuSn_3$ clusters. Reduction pathways on isolated $Cu_{4-n}Sn_n$ ($n = 1–3$) clusters (light purple) and clusters supported on graphene (blue) and on the partially hydroxylated (110) surface of γ-Al_2O_3 (orange).

Fig. 10 Overpotential for the electrocatalytic formation of CO, HCOOH and H_2 on (b) isolated Cu_nSn_{2-n}, (b) Cu_nSn_{2-n}/graphene, and (c) γ-Al_2O_3.

usually higher than that of CO$_2$R due to its much lower overpotential on most metallic catalysts. It was proposed that Sn could weaken the binding strength of H suppressing the HER.[14] Therefore, we have also computed the free energy of H adsorption (ΔG_{H^*}) on the Cu and Cu–Sn clusters to determine the role of Sn incorporation in the selectivity towards the CO$_2$R rather than the HER. In Fig. 9(a), for the isolated Cu and Cu–Sn clusters the H adsorption is favorable on Cu_4 ($\Delta G_{H^*} = -0.19$ eV), Cu_3Sn (-0.45 eV), and $CuSn_3$ (-0.21 eV). In comparison, the value of ΔG_{H^*} computed at the DFT-PBE level of theory for the copper (100) surface is -0.21 eV.[54] On the other hand, Cu_2Sn_2 has the highest Gibbs free energy of H adsorption (0.55 eV). The order from least to most favorable for the HER is Cu_2Sn_2 > Cu_4 > $CuSn_3$ > Cu_3Sn. For the clusters supported on graphene, Fig. 9(b), Cu_2Sn_2 has, again, a positive free energy ($\Delta G_{H^*} = 0.50$ eV), while the H adsorption is favorable on Cu_4 ($\Delta G_{H^*} = -0.60$ eV), Cu_3Sn ($\Delta G_{H^*} = -0.30$ eV) and $CuSn_3$ ($\Delta G_{H^*} = -0.18$ eV). The order from least to most favorable for the HER is Cu_2Sn_2/graphene > $CuSn_3$/graphene > Cu_3Sn/graphene > Cu_4/graphene. Similarly, for the clusters supported on γ-Al_2O_3, Fig. 9(c), Cu_2Sn_2 has the highest Gibbs free energy for H adsorption ($\Delta G_{H^*} = 0.66$ eV). The H adsorption is favorable on Cu_4 ($\Delta G_{H^*} = -0.07$ eV), Cu_3Sn ($\Delta G_{H^*} = -0.20$ eV), and $CuSn_3$ ($\Delta G_{H^*} = -0.72$ eV). The order from least to most favorable for the HER is Cu_2Sn_2/γ-Al_2O_3 > Cu_4/γ-Al_2O_3 > Cu_3Sn/γ-Al_2O_3 > $CuSn_3$/γ-Al_2O_3. Overall, for both gas-phase and supported clusters, Cu_2Sn_2 is highly unfavorable towards HER.

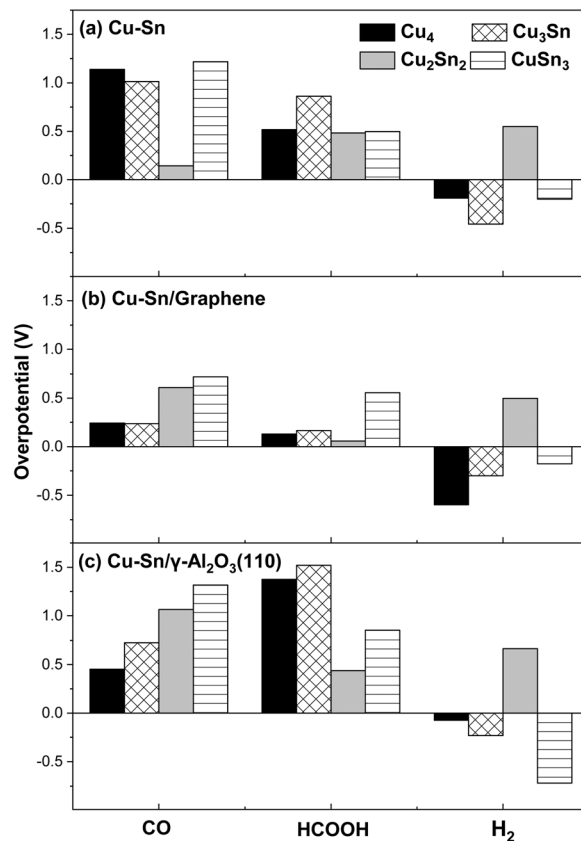**3.4.3 Selectivity.** The limiting potential (U_L) and the overpotential (η) are important factors for evaluating the catalytic activity of eCO$_2$R electrocatalysts.[55] The limiting potential is given by the formula

$$U_L = -\Delta G_{max}/ne \qquad (6)$$

where ΔG_{max} is the free energy change of the rate-determining step at $U = 0$ V, n is the number of electrons transferred, and e is the electron charge. The overpotential (η) can then be obtained from the difference between the equilibrium potential (U_{eq}) and the limiting potential (U_L), which represents the minimum applied potential required to facilitate the formation of relevant intermediates:

$$\eta = U_{eq} - U_L \qquad (7)$$

The magnitudes of the overpotential of the Cu–Sn catalysts for the eCO$_2$R to CO, HCOOH and H$_2$ are summarized in Fig. 10(a–c). Poor catalytic performance towards a specific reaction is associated with a larger overpotential, and *vice versa*.

The eCO$_2$R on the isolated Cu_2Sn_2 cluster displays high selectivity towards CO since it has low overpotential (high catalytic activity) for CO formation (0.14 V) and high overpotential for H$_2$ (0.55 V) and HCOOH (0.48 V) formation (low catalytic activity). The Cu_2Sn_2 catalyst could significantly enhance carbon monoxide selectivity because it is both less

This journal is © the Owner Societies 2023

Phys. Chem. Chem. Phys., 2023, **25**, 13429–13441 | **13439**

selective to formic acid and suppresses HER. CO is the key intermediate in the mechanism of eCO_2R on copper-based catalysts for the generation of C_1 and C_{2+} value-added chemicals such as methane, methanol, ethanol, ethylene, and others.[3] On graphene, however, Cu_2Sn_2 has the lowest overpotential for HCOOH (0.06 V) compared to the relatively high overpotential for CO (0.61 V) and H_2 (0.50 V) formation and, consequently, Cu_2Sn_2 is selective towards formic acid. Of the γ-Al_2O_3 supported clusters, Cu_2Sn_2 has the lowest overpotential for HCOOH (0.44 V). However, it is more susceptible to the HER, as the overpotential for H_2 formation is only slightly higher (0.66 V). The other clusters show negative overpotentials for the HER and therefore are unlikely to be selective towards the eCO_2R reaction. Overall, these results show the combined effects of the composition of the cluster and its supporting material on the selectivity towards CO, HCOOH or H_2.

4. Conclusions

In this work, we conducted density functional theory calculations to characterize the properties of pristine $Cu_{4-n}Sn_n$ (n = 0–4) clusters and their ability to absorb, activate, and convert CO_2 to carbon monoxide (CO) and formic acid (HCOOH). We have divided the discussion of the calculations into four sections: (a) structure, stability, and electronic properties of $Cu_{4-n}Sn_n$ clusters; (b) CO_2 binding and activation over the most stable systems; (c) kinetics of the gas phase CO_2 direct dissociation on $Cu_{4-n}Sn_n$ clusters to generate CO; and (d) liquid-phase electrochemical CO_2 reduction reactions to CO and HCOOH on $Cu_{4-n}Sn_n$ clusters and graphene and γ-Al_2O_3 supported Cu–Sn clusters and their competition with the hydrogen evolution reaction. The energy descriptors, binding energy per atom and the second-order difference in energy, identify Cu_2Sn_2 as the most stable cluster. The electronic energy descriptor HOMO–LUMO gap also suggests that the reactivity of the pure copper cluster, Cu_4, is maintained for Cu_2Sn_2 compared to the other Cu–Sn systems. Moreover, Cu_2Sn_2 activates CO_2 as shown by pronounced bending of the linear O=C=O molecule. Calculations of the free energies for CO_2 reduction pathways to HCOOH and CO show that the isolated Cu_2Sn_2 system has the highest potential as a stable and selective catalyst for the electrochemical CO_2 conversion to CO. But when supported on γ-Al_2O_3 and graphene, the electrochemical CO_2 reduction on Cu_2Sn_2 favors HCOOH formation, particularly over the Cu_2Sn_2/graphene catalyst. In addition, Cu_2Sn_2 suppresses hydrogen evolution reaction. We can conclude that the isolated Cu_2Sn_2 system has the highest potential as a stable and selective catalyst for the electrochemical CO_2 conversion to CO. When supported on graphene and γ-Al_2O_3 (110) surfaces, Cu_2Sn_2 can selectively generate HCOOH.

Author contributions

Conceptualisation of work: AM, AGN and DDT; conduction of computations: AM and QZ; data analyses: AM and AGN, AR; data dissemination & graphics: AM and DDT; writing of the manuscript: AM, AGN and DDT; project support: AR, DDT.

Data availability

Raw data were generated at Queen Mary's Apocrita HPC facility. Derived data supporting the findings of this study are available from the corresponding author (DDT) on request.

Conflicts of interest

The authors declare that the research was conducted in the absence of any commercial or financial relationships that could be construed as a potential conflict of interest.

Acknowledgements

References

1 Y.-X. Duan, F.-L. Meng, K.-H. Liu, S.-S. Yi, S.-J. Li, J.-M. Yan and Q. Jiang, *Adv. Mater.*, 2018, **30**, 1706194.

2 J. Houghton, *Rep. Prog. Phys.*, 2005, **68**, 1343–1403.

3 S. Nitopi, E. Bertheussen, S. B. Scott, X. Liu, A. K. Engstfeld, S. Horch, B. Seger, I. E. L. Stephens, K. Chan, C. Hahn, J. K. Nørskov, T. F. Jaramillo and I. Chorkendorff, *Chem. Rev.*, 2019, **119**, 7610–7672.

4 R. Kortlever, J. Shen, K. J. P. Schouten, F. Calle-Vallejo and M. T. M. Koper, *J. Phys. Chem. Lett.*, 2015, **6**, 4073–4082.

5 X. Chen, J. Chen, N. M. Alghoraibi, D. A. Henckel, R. Zhang, U. O. Nwabara, K. E. Madsen, P. J. A. Kenis, S. C. Zimmerman and A. A. Gewirth, *Nat. Catal.*, 2021, **4**, 20–27.

6 Q. Lu and F. Jiao, *Nano Energy*, 2016, **29**, 439–456.

7 B. Yang, C. Liu, A. Halder, E. C. Tyo, A. B. F. Martinson, S. Seifert, P. Zapol, L. A. Curtiss and S. Vajda, *J. Phys. Chem. C*, 2017, **121**, 10406–10412.

13440 | *Phys. Chem. Chem. Phys.*, 2023, **25**, 13429–13441

This journal is © the Owner Societies 2023

8 C. Liu, B. Yang, E. Tyo, S. Seifert, J. DeBartolo, B. von Issendorff, P. Zapol, S. Vajda and L. A. Curtiss, *J. Am. Chem. Soc.*, 2015, **137**, 8676–8679.

9 P. S. Sai Prasad, J. W. Bae, K.-W. Jun and K.-W. Lee, *Catal. Surv. Asia*, 2008, **12**, 170–183.

10 G. M. Tomboc, S. Choi, T. Kwon, Y. J. Hwang and K. Lee, *Adv. Mater.*, 2020, **32**, 1908398.

11 C. Liu, T. R. Cundari and A. K. Wilson, *J. Phys. Chem. C*, 2012, **116**, 5681–5688.

12 M. Zhang, Z. Zhang, Z. Zhao, H. Huang, D. H. Anjum, D. Wang, J. He and K.-W. Huang, *ACS Catal.*, 2021, **11**, 11103–11108.

13 Q. Li, X. Rao, J. Sheng, J. Xu, J. Yi, Y. Liu and J. Zhang, *J. CO2 Util.*, 2018, **27**, 48–59.

14 M. Morimoto, Y. Takatsuji, R. Yamasaki, H. Hashimoto, I. Nakata, T. Sakakura and T. Haruyama, *Electrocatalysis*, 2018, **9**, 323–332.

15 H. Shin, K. U. Hansen and F. Jiao, *Nat. Sustain.*, 2021, **4**, 911–919.

16 H. Tao, Y. Li, X. Cai, H. Zhou, Y. Li, W. Lin, S. Huang, K. Ding, W. Chen and Y. Zhang, *J. Phys. Chem. C*, 2019, **123**, 24118–24132.

17 J. A. Rodriguez, J. Evans, L. Feria, A. B. Vidal, P. Liu, K. Nakamura and F. Illas, *J. Catal.*, 2013, **307**, 162–169.

18 A. Halder, L. A. Curtiss, A. Fortunelli and S. Vajda, *J. Chem. Phys.*, 2018, **148**, 110901.

19 L. E. Gálvez-González, J. O. Juárez-Sánchez, R. Pacheco-Contreras, I. L. Garzón, L. O. Paz-Borbón and A. Posada-Amarillas, *Phys. Chem. Chem. Phys.*, 2018, **20**, 17071–17080.

20 A. Alvarez-Garcia, E. Flórez, A. Moreno and C. Jimenez-Orozco, *Mol. Catal.*, 2020, **484**, 110733.

21 Megha, K. Mondal, T. K. Ghanty and A. Banerjee, *J. Phys. Chem. A*, 2021, **125**, 2558–2572.

22 S. Yin, T. Swift and Q. Ge, *Catal. Today*, 2011, **165**, 10–18.

23 C. Liu, H. He, P. Zapol and L. A. Curtiss, *Phys. Chem. Chem. Phys.*, 2014, **16**, 26584–26599.

24 F. Huang, Y. Deng, Y. Chen, X. Cai, M. Peng, Z. Jia, J. Xie, D. Xiao, X. Wen, N. Wang, Z. Jiang, H. Liu and D. Ma, *Nat. Commun.*, 2019, **10**, 4431.

25 L. Jin, B. Liu, P. Wang, H. Yao, L. A. Achola, P. Kerns, A. Lopes, Y. Yang, J. Ho, A. Moewes, Y. Pei and J. He, *Nanoscale*, 2018, **10**, 14678–14686.

26 J.-C. Liu, H. Xiao, X.-K. Zhao, N.-N. Zhang, Y. Liu, D.-H. Xing, X. Yu, H.-S. Hu and J. Li, *CCS Chem.*, 2022, **5**, 152–163.

27 D. Yang, S. Zuo, H. Yang, Y. Zhou, Q. Lu and X. Wang, *Adv. Mater.*, 2022, **34**, 2107293.

28 N. Sakamoto, Y. F. Nishimura, T. Nonaka, M. Ohashi, N. Ishida, K. Kitazumi, Y. Kato, K. Sekizawa, T. Morikawa and T. Arai, *ACS Catal.*, 2020, **10**, 10412–10419.

29 D. Du, H. Zhu, Y. Guo, X. Hong, Q. Zhang, B. Suo, W. Zou and Y. Li, *J. Phys. Chem. C*, 2022, **126**, 11611–11618.

30 G. Kresse and J. Furthmüller, *Comput. Mater. Sci.*, 1996, **6**, 15–50.

31 J. P. Perdew, K. Burke and M. Ernzerhof, *Phys. Rev. Lett.*, 1996, **77**, 3865–3868.

32 S. Grimme, J. Antony, S. Ehrlich and H. Krieg, *J. Chem. Phys.*, 2010, **132**, 154104.

33 G. Kresse and D. Joubert, *Phys. Rev. B: Condens. Matter Mater. Phys.*, 1999, **59**, 1758–1775.

34 G. Henkelman, B. P. Uberuaga and H. Jónsson, *J. Chem. Phys.*, 2000, **113**, 9901–9904.

35 A. J. Göttle and M. T. M. Koper, *Chem. Sci.*, 2017, **8**, 458–465.

36 J. Rossmeisl, Z. W. Qu, H. Zhu, G. J. Kroes and J. K. Nørskov, *J. Electroanal. Chem.*, 2007, **607**, 83–89.

37 K. Mathew, R. Sundararaman, K. Letchworth-Weaver, T. A. Arias and R. G. Hennig, *J. Chem. Phys.*, 2014, **140**, 84106.

38 Q. Zhang and A. Asthagiri, *Catal. Today*, 2019, **323**, 35–43.

39 H. A. Hansen, J. B. Varley, A. A. Peterson and J. K. Nørskov, *J. Phys. Chem. Lett.*, 2013, **4**, 388–392.

40 C. J. Pickard and R. J. Needs, *J. Phys.: Condens. Matter*, 2011, **23**, 53201.

41 V. V. Albert, S. A. Ivanov, S. Tretiak and S. V. Kilina, *J. Phys. Chem. C*, 2011, **115**, 15793–15800.

42 L. Tan, C. J. Pickard, K. Yu, A. Sapelkin, A. J. Misquitta and M. T. Dove, *J. Phys. Chem. C*, 2019, **123**, 29370–29378.

43 J. Gu, J. Wang and J. Leszczynski, *ACS Omega*, 2018, **3**, 1881–1888.

44 G. Paglia, C. E. Buckley, A. L. Rohl, R. D. Hart, K. Winter, A. J. Studer, B. A. Hunter and J. V. Hanna, *Chem. Mater.*, 2004, **16**, 220–236.

45 M. Yamamoto, Q. Zhao, S. Goto, Y. Gu, T. Toriyama, T. Yamamoto, H. Nishihara, A. Aziz, R. Crespo-Otero, D. D. Tommaso, M. Tamura, K. Tomishige, T. Kyotani and K. Yamazaki, *Chem. Sci.*, 2022, **13**, 3140–3146.

46 J. Gross, *J. Chem. Phys.*, 2009, **131**, 204705.

47 K. Jug, B. Zimmermann, P. Calaminici and A. M. Köster, *J. Chem. Phys.*, 2002, **116**, 4497–4507.

48 W. Tang, E. Sanville and G. Henkelman, *J. Phys.: Condens. Matter*, 2009, **21**, 084204.

49 G. Henkelman, A. Arnaldsson and H. Jónsson, *Comput. Mater. Sci.*, 2006, **36**, 354–360.

50 E. Sanville, S. D. Kenny, R. Smith and G. Henkelman, *J. Comput. Chem.*, 2007, **28**, 899–908.

51 S.-G. Wang, X.-Y. Liao, D.-B. Cao, C.-F. Huo, Y.-W. Li, J. Wang and H. Jiao, *J. Phys. Chem. C*, 2007, **111**, 16934–16940.

52 M. Xing, L. Guo and Z. Hao, *Dalton Trans.*, 2019, **48**, 1504–1515.

53 J. Niu, J. Ran, Z. Ou, X. Du, R. Wang, W. Qi and P. Zhang, *J. CO2 Util.*, 2016, **16**, 431–441.

54 A. G. Nabi, A. ur-Rehman, A. Hussain and D. D. Tommaso, *Mol. Catal.*, 2022, **527**, 112406.

55 J.-H. Liu, L.-M. Yang and E. Ganz, *J. Mater. Chem. A*, 2019, **7**, 11944–11952.

This journal is © the Owner Societies 2023

Phys. Chem. Chem. Phys., 2023, **25**, 13429–13441 | 13441